Zircon Solubility in Solute-Rich Supercritical Fluids and Zr Transfer From Slab to Wedge in the Deep Subduction Process

3 authors, including:

Chen Wei
Chinese Academy of Sciences
5 PUBLICATIONS **30** CITATIONS

SEE PROFILE

Eiichi Takahashi
Chinese Academy of Sciences
175 PUBLICATIONS **9,159** CITATIONS

SEE PROFILE

Some of the authors of this publication are also working on these related projects:

Project   Zr and Hf mobility and fractionation in subduction zones View project

Project   The partitioning behaviors of the first-row transition elements during magma processes View project

Key Points:
- Zircon solubility in solute-rich supercritical fluids is 10–100 times higher than that in dilute aqueous fluids
- Zircon solubility increases most prominently with the solute content and alkali/Al ratio in supercritical fluids
- Slab-derived solute-rich and high-alkali supercritical fluids play an important role in Zr transfer in subduction zones

Zircon Solubility in Solute-Rich Supercritical Fluids and Zr Transfer From Slab to Wedge in the Deep Subduction Process

Wei Chen[1,2,3,5], **Xiaolin Xiong**[1,2,4,5], **and Eiichi Takahashi**[1,2]

[1]State Key Laboratory of Isotope Geochemistry, Guangzhou Institute of Geochemistry, Chinese Academy of Sciences, Guangzhou, China, [2]CAS Center for Excellence in Deep Earth Science, Guangzhou, China, [3]Deep Sea Research Center, Institute of Oceanology, Chinese Academy of Sciences, Qingdao, China, [4]Southern Marine Science and Engineering Guangdong Laboratory (Guangzhou), Guangzhou, China, [5]College of Earth and Planetary Sciences, University of the Chinese Academy of Sciences, Beijing, China

Abstract Zircon solubility in aqueous fluids, hydrous melts, and supercritical fluids is important for understanding the high field strength elements (HFSEs) chemical transport in subduction zones. Although zircon solubility was extensively studied in aqueous fluids and hydrous silicate melts, its solubility in solute-rich fluids or supercritical fluids is poorly known. Here, we experimentally determined zircon solubility in $KAlSi_3O_8$ ($\pm K_2O \pm Al_2O_3$) – H_2O supercritical fluids at 2.0–6.0 GPa and 800°C–1000°C, close to the slab-top conditions at sub-arc depths. The results show that zircon solubility (expressed as ZrO_2 content at zircon saturation) ranges from 65 to 6,400 ppm ZrO_2, 10–100 times higher than that in dilute aqueous fluids; it increases with temperature, solute content, and solute alkalinity (molar K/Al ratio) but decreases with pressure. The experiments at 2.0 GPa show that solute alkalinity in addition to temperature and solute content exerts a primary control on zircon solubility, while the experiments at 4.0–6.0 GPa show that the negative effect of pressure on zircon solubility is offset by the increase in solute alkalinity due to the crystallization of Al-rich phases kyanite and muscovite. We suggest that high-alkali supercritical fluids during deep subduction could be significant transfer agents for Zr from slab to mantle wedge.

Plain Language Summary High field strength elements (HFSEs), such as Zr, Hf, Ti, Nb, and Ta, are traditionally considered to be immobile in shallow geological processes. However, the ubiquitous presence of zircon and rutile (the hosts of HFSEs) in high-pressure metamorphic veins and orogenic peridotites provides compelling evidence that HFSEs are transportable in subduction zones. The transfer reagents of HFSEs in subduction zones include aqueous fluids, hydrous melts, and supercritical fluids. Experimental solubility data on zircon and rutile in aqueous fluids and hydrous melts are abundant, but remain scarce in supercritical fluids, which has stymied a thorough understanding of the HFSEs transfer in subduction zones. This study experimentally determined zircon solubility in $KAlSi_3O_8$ ($\pm K_2O \pm Al_2O_3$) – H_2O supercritical fluids at 2.0–6.0 GPa and 800–1000°C, close to the slab-top conditions at sub-arc depths. The results show that zircon solubility in supercritical fluids is 10–100 times higher than that in dilute aqueous fluids and increases dominantly with the solute content and alkali/Al ratio in supercritical fluids. Therefore, solute-rich and high-alkali supercritical fluids during deep subduction could be efficient transfer agents for Zr and other HFSEs and any models involved in chemical transfer in subduction zones should consider the role of supercritical fluids.

1. Introduction

Zircon and rutile are common accessory minerals in igneous rocks and metamorphic rocks. Phase equilibrium experiments (Klimm et al., 2008; Rustioni et al., 2019; Xiong et al., 2009) suggest that they are refractory during slab dehydration or melting, and thus largely control the budget of high field strength elements (HFSEs) in the released fluids/melts and residual eclogites (e.g., Hermann & Rubatto, 2009). The characteristic depletion of HFSEs in arc magmas is usually explained by the hypothesis that the fluids released from subducting slabs are enriched in incompatible elements, while the residual minerals zircon and rutile sequester and retain HFSEs. Early experiments on zircon and rutile solubility suggested that they

were soluble in aqueous fluids (Ayers & Watson, 1991), but their results were significantly overestimated due to a large capsule design (Tropper & Manning, 2005). More recent experiments gave extremely low solubility of zircon and rutile in dilute aqueous fluids (Audétat & Keppler, 2005; Antignano & Manning, 2008; Bernini et al., 2013; Tropper & Manning, 2005), which is consistent with the "conservative" nature of these elements in shallow geological processes. However, the ubiquitous presence of zircon and rutile in orogenic peridotites (Faithfull et al., 2018; Kalfoun et al., 2002; Li et al., 2016; Malaspina et al., 2006) and as daughter minerals of fluid inclusions and vein minerals in high-pressure and ultrahigh-pressure metamorphic rocks (Ferrando et al., 2005; Gao et al., 2007; Rubatto & Hermann, 2003; Zhang et al., 2008) provides compelling evidence that HFSEs are soluble and transportable in fluids, making the paradigm "HFSE immobility in subduction zones" no longer tenable.

In subduction zones, the mobile phases for elements transfer include aqueous fluid, hydrous melt, and supercritical fluid (Kessel et al., 2005; Li & Ni, 2020; Ni et al., 2017). The nature and composition of these mobile phases derived from slabs change with subduction depth due to increasing pressure and temperature. At temperatures below the solidus of a rock-H_2O system, only aqueous fluid coexists with solid minerals; above this temperature, melting occurs, and thus hydrous melt ± aqueous fluid coexists with solid minerals. With increasing pressure and temperature, the immiscibility gap between aqueous fluid and hydrous melt diminishes and finally closes due to the mutually enhanced solubilities of H_2O in silicate melt and silicate in H_2O (e.g., Manning, 2004; Ni et al., 2017), forming a solute-rich supercritical fluid beyond the second critical endpoint where the wet solidus and critical curve intersect. The supercritical phenomenon between hydrous silicate melt and aqueous fluid has been observed in situ and confirmed in high *P-T* experiments (Bureau & Keppler, 1999; Kawamoto et al., 2012; Mibe et al., 2008; Shen & Keppler, 1997). Field studies have also suggested that the multiphase inclusions in UHP rocks represent solute-rich supercritical fluids produced during metamorphism (Ferrando et al., 2005; Zhang et al., 2008). Therefore, supercritical fluid may be prevalent during deep subduction and responsible for chemical transport in subduction zones (Kessel et al., 2005; Zheng & Hermann, 2014).

As the two most important host minerals for HFSEs, the solubility of zircon and rutile in hydrous melts and aqueous fluids has been widely investigated (Borisov & Aranovich, 2019; Gervasoni et al., 2016, and references therein). Experiments with hydrous melts indicate that composition and temperature are the two dominant controls on the solubility of zircon and rutile (e.g., Linnen & Keppler, 2002; Watson & Harrison, 1983; Xiong et al., 2005, 2009). Experiments with aqueous fluids suggest that Zr complexes with alkali-silicates to form polymeric species when the total amount of dissolved solute >10 wt.% (Louvel et al., 2013; Wilke et al., 2012), and further addition of alkali-silicate into such fluids greatly enhances the solubility of HFSEs (Bernini et al., 2013; Wilke et al., 2012). Supercritical fluids are solute-rich and thus are potentially more effective for the transfer of HFSEs in subduction zones. Recent experiments (Chen et al., 2018; Hayden & Manning, 2011) show that rutile solubility in supercritical fluids increases with solute content and is much higher than that in dilute aqueous fluids. Kessel et al. (2005) performed experiments to investigate the trace element signature of subduction-zone fluids, melts, and supercritical liquids. Their results show that Zr partition coefficient ($D_{Zr}^{liquid/solid}$) between supercritical fluid and eclogitic residue is clearly higher than that between aqueous fluid and eclogitic residue, implying that zircon may be soluble in solute-rich supercritical fluids. To our knowledge, experimental data on zircon solubility in solute-rich supercritical fluids remain scarce, especially over typical slab-top conditions, and a relevant study is thus necessary.

In this study, we performed piston-cylinder and multi-anvil experiments at 2.0–6.0 GPa and 800°C–1000°C, which are close to the slab-top *P-T* conditions at sub-arc depths, to investigate zircon solubility in supercritical $KAlSi_3O_8$ ($\pm K_2O \pm Al_2O_3$) – H_2O fluids. The fluids are solute-rich (35–88 wt.%) and slightly peraluminous to strongly peralkaline, as reasonable analogs of sediment-derived supercritical fluids. The experimental results allow us to assess the effects of *T*, *P*, solute content, and alkalinity (alkali/Al) on zircon solubility and to elucidate the role of supercritical fluids in the migration of Zr in subduction zones.
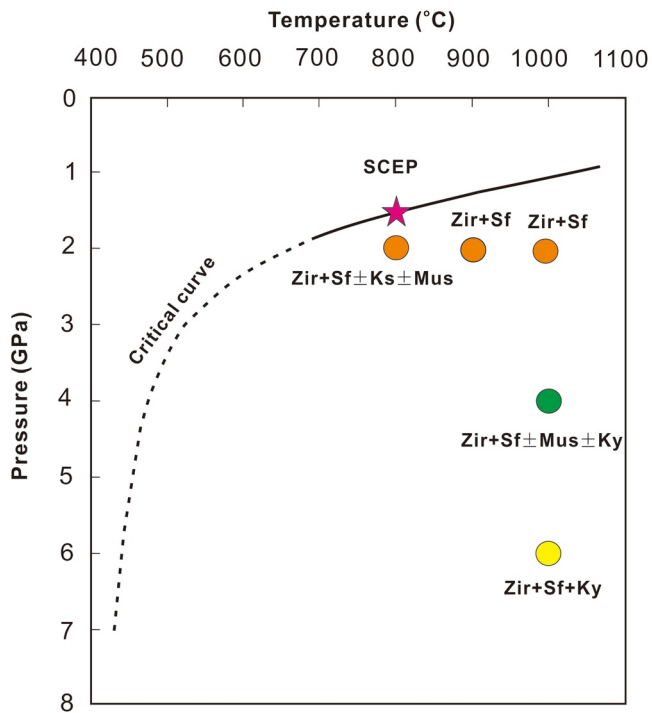
Figure 1. Critical curve of the $KAlSi_3O_8$-H_2O system (Mibe et al., 2008) and experimental *P-T* points and run products (this study), showing the experimental *P-T* conditions beyond the critical curve. Abbreviations: Kf, K-feldspar; Ky, Kyanite; Mus, muscovite; SCEP, Second Critical End Point; Sf, Supercritical fluid; Zir, Zircon.

2. Experimental and Analytical Methods

2.1. Starting Materials and Sample Capsules

To investigate zircon solubility in supercritical fluids, we chose $KAlSi_3O_8$ ($\pm K_2O \pm Al_2O_3$) as the solute. This is because (a) silicon, aluminum, and alkalis are the most abundant solute components in subduction zone fluids (Manning, 2004; Schmidt, 2015), (b) K-rich felsic compositions represent a first-order approximation of the compositions of hydrous melts that are experimentally derived from sediments (Hermann & Rubatto, 2009; Schmidt, 2015), and (c) the phase relationship (Figure 1) and supercritical behavior in the $KAlSi_3O_8$-H_2O system have been well constrained by in situ observations in a hydrothermal diamond anvil cell (HDAC) (Mibe et al., 2008).

The $KAlSi_3O_8$ starting composition was synthesized from a stoichiometric mixture of K_2CO_3 and analytical grade oxides Al_2O_3 and SiO_2. The mixture was first ground under ethanol in an agate mortar for 2 h, sintered in a Pt crucible at 1000°C for 10 h to remove CO_2, and then fused at 1400°C for 3 h. The quenched glass was ground to powder. The fine powder was then mixed with 2.97 wt.% ZrO_2 and ground again for 3 h. This ZrO_2-bearing $KAlSi_3O_8$ composition (molar K/Al = 1.0) was designed to investigate the effects of *T*, *P*, and solute content on zircon solubility. To investigate the effect of solute composition (alkalinity), we also prepared another two starting compositions with molar K/Al ratios of 0.90 and 1.38 from ZrO_2-bearing $KAlSi_3O_8$ basic glass using the same procedure described above.

Au capsules (length of ∼5.0 mm, ID of 1.8 mm, and OD of 2.0 mm) were used for all the experiments. The use of short capsules (further compressed to less than 4 mm during the experiment) efficiently reduced the temperature gradient along the sample capsule during the experiment. Experiments involved a total of 10–60 wt.% H_2O. To adjust the glass powder to H_2O ratio, approximately 10 mg of glass powder were loaded with 1.1–15 μL of deionized H_2O, injected into the capsule with a micro-syringe before the solid powder was loaded. After loading, the capsule was crimped and welded shut with the LAMPERT PUK U3 welding machine. During the welding, the capsule was immersed in wet tissue paper to avoid significant H_2O loss. All capsules were checked by weighing before and after welding and then they were stored in an oven at 120°C for at least 5 h and weighed again to check weight loss. Any capsule with evident mass loss after the two-round weighing check was discarded.

2.2. High-Temperature and High-Pressure Experiments

The experiments were performed at 2.0–6.0 GPa and 800°C–1000°C (Table 1), which are well above the critical curve of the $KAlSi_3O_8$-H_2O system (Figure 1). High-pressure equipments were a solid media piston-cylinder apparatus and a multi anvil press installed at State Key Laboratory of Isotope Geochemistry, Guangzhou Institute of Geochemistry, Chinese Academy of Sciences. At 2.0 GPa, experiments were conducted with a Rockland piston-cylinder apparatus using 1/2 inch assemblies consisting of a graphite furnace + $BaCO_3$ sleeve + MgO inserts. A friction correction of 13% was applied to the nominal pressure based on a calibration of the quartz-coesite transition, and the pressure uncertainty was believed to be within ±0.1 GPa (Chen et al., 2021). The experimental temperature was monitored with S-type thermocouples and was controlled to within ±2°C of the set-point using a Eurotherm controller. At 4.0 and 6.0 GPa, a 2,500-ton Kawai-type multi-anvil press was used to compress the octahedra using 25 mm edge-length WC anvils with 15 mm corner truncations. The pressure calibration was performed using the phase transitions of Bi metal at room temperature. A Cr_2O_3-doped MgO multi-anvil octahedron of 25 mm edge length was employed with a lanthanum chromate heater. A MgO sleeve was used to separate the capsule from the furnace, and a disk of Al_2O_3 was placed between the thermocouple and the top of the capsule. The temperature

Table 1
Experimental Conditions and Run Products

Run No	Solute	[a]H_2O (wt.%)	P (GPa)	T (°C)	Duration (h)	Zir	Sf	Kf	Mus	Ky	**H_2O	*H_2O
Series 1: $KAlSi_3O_8$-H_2O system (2.97 wt.% ZrO_2 in initial $KAlSi_3O_8$ solute)												
AZ1	$KAlSi_3O_8$	11.5	2	1000	96	4.30	95.7				12.0	6.5
AZ2	$KAlSi_3O_8$	22.0	2	1000	96	3.55	96.5				22.8	8.9
AZ3	$KAlSi_3O_8$	30.5	2	1000	96	3.15	96.9				31.5	11.1
AZ4	$KAlSi_3O_8$	40.1	2	1000	96	2.69	97.3				41.2	15.8
AZ5	$KAlSi_3O_8$	50. 5	2	1000	96	2.24	97.8				51.6	16.2
AZ6	$KAlSi_3O_8$	60.3	2	1000	96	1.79	98.2				61.4	14.2
AZ7	$KAlSi_3O_8$	11.9	2	900	120	4.06	96.0				12.4	8.7
AZ8	$KAlSi_3O_8$	21.0	2	900	120	3.83	96.2				21.8	11.9
AZ9	$KAlSi_3O_8$	28.5	2	900	120	3.27	96.7				29.5	8.5
AZ10	$KAlSi_3O_8$	35.2	2	900	120	2.97	97.0				36.3	13.0
AZ11	$KAlSi_3O_8$	52.67	2	900	120	2.26	97.7				53. 9	14.4
[b]AZ12	$KAlSi_3O_8$	9.9	2	800	168	+	+	+			Nd	10.3
[b]AZ13	$KAlSi_3O_8$	21.5	2	800	168	+	+	+			Nd	13.4
AZ14	$KAlSi_3O_8$	29.8	2	800	168	2.09	95.6		2.28		31.1	14.9
AZ15	$KAlSi_3O_8$	37.8	2	800	168	1.85	96.1		2.02		39.3	12.8
AZ18	$KAlSi_3O_8$	11.5	4	1000	96	2.63	94.5		2.87		12.1	8.60
AZ19	$KAlSi_3O_8$	19.8	4	1000	96	2.38	95.0		2.60		20.8	10.7
AZ20	$KAlSi_3O_8$	28.4	4	1000	96	2.13	95.6		2.32		29.7	9.68
AZ21	$KAlSi_3O_8$	40.0	4	1000	96	1.78	96.3			1.95	41.5	32.4
AZ22	$KAlSi_3O_8$	47.9	4	1000	96	1.55	96.8			1.69	49. 5	18.1
AZ23	$KAlSi_3O_8$	61.7	4	1000	96	1.14	97.6			1.24	63.2	60.7
AZ24	$KAlSi_3O_8$	11.2	6	1000	96	4.02	92.9			3.13	12.1	9.97
AZ25	$KAlSi_3O_8$	20.8	6	1000	96	2.35	95.1			2.57	21.9	13.1
AZ26	$KAlSi_3O_8$	53.0	6	1000	96	1.40	97.1			1.52	54.6	13.1
Series 2: $KAlSi_3O_8 \pm Al_2O_3 \pm K_2O$-$H_2O$ system (2.97 wt.% ZrO_2 in the initial $KAlSi_3O_8$ solute)												
AK1	$KAlSi_3O_8 + K_2O$	28.61	2	1000	96	2.37	97.63				29.3	10.9
AK2	$KAlSi_3O_8 + Al_2O_3$	30.55	2	1000	96	3.09	96.91				31.5	15.2

Note. Kf, K-feldspar; Ky, kyanite; Mus, muscovite; nd, not determined; Sf, supercritical fluid; Zir, zircon. "+" indicates presence of a phase, whereas whitespace indicates absence of a phase. **H_2O is the H_2O content in the supercritical fluid (before H_2O exsolution during quenching) calculated from mass balance. *H_2O is the H_2O content in the quenched glass calculated from the difference of solute oxide total from 100%.

[a]H_2O is the bulk H_2O content added to the starting material. [b]Phase proportion cannot be estimated by mass balance calculation in the two runs because the composition of K-feldspar is identical to the starting material.

was monitored using a $W_{95}Re_5$-$W_{74}Re_{26}$ thermocouple inserted axially into the furnace inside an alumina tube. For the piston-cylinder experiments, the temperature gradient over capsule length was estimated to be <20°C. For the multi-anvil experiments, the temperature gradient of a sample capsule measured by two pyroxene thermometers was <7°C/mm. Run durations varied from 4 to 7 days, depending on experimental temperatures. Each run was terminated by turning off power to the heater (temperature dropped to <100°C within 20 s), and then pressure was unloaded slowly.

2.3. Sample Preparation

After an experiment, the capsule was removed from the furnace assembly. No attempt was made to compare the sample capsule with its pre-run weight because previous experiments have shown that it was impossible to avoid corrosion of the metal capsule wall by the pressure media (Chen et al., 2018). The recovered capsules were thus directly pierced with a razor blade. H_2O loss was found in some H_2O-rich runs upon opening, as evidenced by hissing and appearance of H_2O along the incision, indicating H_2O exsolution during quenching. To avoid the potential detachment of quenched glasses from the capsule during sample preparation, two steps were taken: (a) the opened capsules were stored in a drying oven at 110°C for 15 min to remove moisture, and (b) they were longitudinally sectioned with a diamond wire saw and then impregnated with epoxy in vacuum. Finally, two capsule halves from each run were mounted in epoxy and polished for optical observations and chemical analyses.

2.4. Electron Microprobe Analysis

The well-polished sections were carefully observed under an optical microscope and scanning electron microscope before analysis. Compositions (SiO_2, Al_2O_3, K_2O, and ZrO_2) of the minerals (K-feldspar, muscovite, and kyanite) and quenched glasses in run products were analyzed using a JEOL JXA-8230 electron probe micro-analyzer (EPMA) in wavelength dispersive spectrometry mode at State Key Laboratory of Isotope Geochemistry, Guangzhou Institute of Geochemistry, Chinese Academy of Sciences. The analytical conditions for minerals were 15 kV acceleration voltage, 20 nA beam current, and 1 μm beam diameter, and those for quenched glasses were the same voltage, 10 nA beam current, and 10–30 μm beam diameter. The analytical points were positioned over bubble-free (or bubble-poor) glasses as much as possible. A relatively broad beam and low current were used to avoid significant K loss during analyses of H_2O-rich quenched glasses. Monitoring the K_2O signal showed that no significant K loss occurred during the analyses. Peak counting times were 60 s (Si and Zr) and 20 s (Al and K) for minerals and 10 s (K), 30 s (Si and Al), and 60 s (Zr) for glasses. ZAF correction was employed for the raw data. The analytical standards were diopside (Si), corundum (Al), zircon (Zr), and orthoclase (K). To obtain more accurate analyses of ZrO_2 in glasses, we reanalyzed the glasses using a high beam current of 60–100 nA at 15 kV acceleration voltage with the analyzed points (10 μm) at a distance >10 μm from the zircon crystals to avoid the influence of fluorescence from zircon (Linnen & Keppler, 2002). The instrument detection limit of ZrO_2 under this analytical condition is 90 ppm, which is below the ZrO_2 concentrations in most H_2O-rich experiments (where most ZrO_2 > 300 ppm). The analytical errors were typically better than ±1% (SiO_2, Al_2O_3, and K_2O) for minerals and ±1% (SiO_2 and Al_2O_3), ±10% (K_2O), and ±10% (ZrO_2) for glasses.

3. Experimental Results

3.1. Phase Relations

A total of 26 runs were performed. The run products included Zir (zircon) + Sf (supercritical fluid) ± Kf (K-feldspar) ± Mus (muscovite) ± Ky (kyanite). The supercritical fluids were quenched to hydrous glasses that were full of vesicles formed during quenching. The experimental conditions (including the starting solute, H_2O, P, T, and duration) and run products are listed in Table 1. The compositions of the quenched glasses are presented in Table 2, and those of K-feldspar, muscovite, and kyanite are reported in Table 3. Mass balance calculations were used to calculate the phase proportions. The run products contain ∼1.1–4.3 wt.% zircon ($ZrSiO_4$) and ∼92–98 wt.% supercritical fluids, except for runs AZ12 and AZ13, where significant amounts of K-feldspar were crystallized (Table 1); phase proportions in these two runs cannot be estimated from the product compositions because K-feldspar is compositionally identical to the starting material.

Phase proportions in run products are dependent on P, T, and H_2O content. For the runs at 2.0 GPa and 900°C–1000°C, the products only contain Zir + Sf. For the experiments under other conditions, run products contain K-feldspar, muscovite, or kyanite in addition to zircon + Sf. At 2.0 GPa and 800°C, K-feldspar at bulk H_2O ≤ 20 wt.% or muscovite at bulk H_2O ≥ 30 wt.% is present. At 4 GPa and 1000°C, the run products contain muscovite at bulk H_2O ≤ 30 wt.% or kyanite at bulk H_2O ≥ 30 wt.%. At 6 GPa and 1000°C, kyanite is the only crystallization phase in addition to zircon. The presence of K-feldspar and muscovite at 2.0 GPa and 800°C are consistent with the in situ observation of the $KAlSi_3O_8$-H_2O system in the HDAC experiments

Table 2
Composition of the Quenched Glasses (n ≥ 10, SiO_2, Al_2O_3, and K_2O in wt.%)

Run no.	Al_2O_3 AV.	S.D.(1σ)	SiO_2 AV.	S.D.(1σ)	K_2O AV.	S.D.(1σ)	ZrO_2 (ppm) AV.	S.D.(1σ)	Total AV.	S.D.(1σ)	[a]ZrO_2 (ppm) (solubility) AV.	S.D.(1σ)	[c]Molar K/Al
AZ1	16.35	0.17	61.99	1.34	15.10	0.16	714	62	93.52	1.63	671	58	1.00
AZ2	16.05	0.37	60.68	1.52	14.82	0.34	676	63	91.62	1.88	569	53	1.00
AZ3	15.50	0.24	59.08	0.64	14.32	0.22	518	36	88.95	0.92	399	28	1.00
AZ4	14.76	0.99	55.78	3.11	13.64	0.91	484	33	84.23	1.20	338	23	1.00
AZ5	16.44	0.33	62.13	1.59	15.18	0.30	382	33	93.79	1.53	197	17	1.00
AZ6	16.43	0.25	64.19	0.61	15.17	0.23	375	21	95.83	0.16	151	8	1.00
AZ7	16.20	0.11	59.84	0.19	15.28	0.17	323	35	91.35	0.24	310	34	1.00
AZ8	15.52	0.38	57.82	1.35	14.77	0.22	267	21	88.14	1.89	237	18	1.00
AZ9	16.17	0.15	60.03	0.29	15.30	0.24	280	14	91.53	0.51	216	11	1.00
AZ10	15.33	0.20	57.64	0.73	14.04	0.23	144	13	87.02	0.96	106	9	1.00
AZ11	14.94	0.63	56.86	2.03	13.80	0.58	120	28	85.61	0.16	65	15	1.00
[b]AZ12	15.51	0.18	59.06	0.55	15.14	0.26	110	21	89.73	0.79	nd[b]		
[b]AZ13	15.93	0.21	56.45	0.51	14.18	0.20	166	36	86.57	0.67	nd[b]		
AZ14	15.05	0.12	55.56	0.44	14.45	0.18	184	31	85.08	0.16	149	25	1.04
AZ15	15.94	0.21	56.01	0.33	15.21	0.16	133	22	87.18	1.16	93	15	1.03
AZ18	16.08	0.14	59.46	0.34	15.54	0.22	657	83	91.15	0.46	638	81	1.05
AZ19	15.26	0.22	58.67	0.64	15.36	0.27	514	67	89.33	1.01	456	59	1.09
AZ20	16.03	0.16	58.84	0.37	15.40	0.28	497	62	90.32	0.46	387	49	1.04
AZ21	10.30	0.24	41.24	0.68	15.98	0.18	385	58	67.56	1.46	333	50	1.68
AZ22	14.20	0.29	53.51	0.74	14.13	0.58	295	36	81.87	2.46	182	22	1.08
AZ23	6.26	0.98	26.56	2.84	6.49	0.56	110	10	39.32	3.46	103	9	1.12
AZ24	11.47	1.54	61.98	2.82	16.45	1.64	1,230	151	90.03	1.67	1202	148	1.55
AZ25	10.28	0.34	59.97	0.67	16.57	0.13	968	91	86.92	2.67	870	81	1.75
AZ26	5.75	0.52	66.13	1.43	14.99	0.27	372	40	86.91	1.13	194	21	2.82
AK1	15.93	0.34	52.12	0.85	20.31	0.40	8,029	261	89.16	0.87	6367	207	1.38
AK2	16.88	0.55	53.98	0.39	13.88	1.03	478	49	84.79	0.91	356	40	0.89

[a]ZrO_2 (ppm, zircon solubility) in supercritical fluids were calculated with $X_{Zr} = X_{Zr}^{measured} \cdot (100 - **H_2O)/Total^{measured}$, where X_{Zr} is the ZrO_2 concentration in supercritical fluid; $X_{Zr}^{measured}$ is the ZrO_2 concentration in quenched glass determined by EMPA (column 13 in this Table 1); **H_2O (column 112 in Table 1) is the H_2O concentration (wt.%) in supercritical fluid calculated from mass balance. [b]nd = not determined due to K-feldspar crystallization leading to no way to determine the H_2O content of the supercritical fluid. [c]K/Al = molar K_2O/Al_2O_3.

(Mibe et al., 2008); the phase assemblages containing muscovite and kyanite at 4.0–6.0 GPa and 1000°C are also comparable with experimental results using metapelite and greywacke as starting materials under similar *P-T* conditions (M. W. Schmidt et al., 2004), although the simplified $KAlSi_3O_8$-H_2O system is adopted in this study. All the experimental *P-T* conditions were beyond the critical curve of the $KAlSi_3O_8$-H_2O system (Figure 1); thus, all the fluids in the runs with only zircon ± K-feldspar crystallization were supercritical. For the runs with muscovite or kyanite crystallization, the solute compositions became K_2O-rich (molar K/Al = ~1.05–2.82, Table 2) since both of these phases are Al-rich (Table 3) (muscovite [$KAl_3Si_3O_{10}(OH)_{10}$, K/Al = ~0.32] and kyanite-rich [Al_2SiO_5, containing nearly no K]). The alkali-rich solute compositions (Bureau & Keppler, 1999) should have critical curves located at lower P-T conditions than the $KAlSi_3O_8$-H_2O system. Likewise, the experimental conditions with the $KAlSi_3O_8 + K_2O + H_2O$ composition should also be above the critical curve. Even for the experiment with a $KAlSi_3O_8 + Al_2O_3 + H_2O$ composition, non-supercritical behavior was not observed because the solute composition was only slightly peraluminous (K/Al = 0.91).

Table 3
Composition of the Minerals (wt.%, n ≥ 10)

Run no.	Mineral	Al_2O_3		SiO_2		K_2O		Total		K/Al
		AV.	S.D.(1σ)	AV.	S.D.(1σ)	AV.	S.D.(1σ)	AV.	S.D.(1σ)	
AZ12	Kf	17.85	0.08	65.11	0.35	17.56	0.06	100.53	0.4	1.007
AZ13	Kf	18.39	0.12	65.23	0.19	16.95	0.1	100.56	0.34	1.000
AZ14	Mus	37.34	0.18	46.99	0.46	11.00	0.55	95.35	0.82	0.320
AZ15	Mus	36.82	0.69	48.08	0.51	10.79	0.27	95.69	0.96	0.318
AZ18	Mus	36.87	0.3	47.38	1.00	11.42	0.26	95.67	0.83	0.336
AZ19	Mus	37.36	0.23	47.01	0.15	10.9	0.23	95.27	0.32	0.317
AZ20	Mus	37.97	0.63	47.27	0.94	10.84	0.37	96.09	1.36	0.310
AZ21	Ky	62.98	0.6	37.4	0.72	0.04	0.02	100.42	1.31	0.001
AZ22	Ky	63.2	0.53	37.7	0.56	0.06	0.03	100.96	1.08	0.001
AZ23	Ky	60.82	0.03	37.29	0.03	Nd	nd	98.11	0.03	0.001
AZ24	Ky	62.04	0.46	37.26	0.32	0.13	0.04	99.42	0.5	0.002
AZ25	Ky	60.14	0.42	37.71	0.23	0.55	0.08	98.4	0.59	0.009
AZ26	Ky	63.20	1.04	37.87	0.53	0.12	0.02	101.19	0.60	0.002

Note. Kf, K-feldspar; Ky, kyanite; Mus, muscovite; nd, not determined; Sf, supercritical fluid; Zir, zircon; K/Al = molar K_2O/Al_2O_3.

3.2. Characteristics of Zircon and Quenched Glasses

Subhedral to euhedral zircon grains (typically <10 μm) occurred in all the runs. Zircon grains vary systematically with temperature, H_2O content, and solute alkalinity. At similar H_2O contents, zircon crystals produced at a high temperature are larger than those produced at a low temperature. At a given temperature, zircon crystals grown at a high H_2O content are larger than those grown at a lower H_2O content. High solute alkalinity is also favorable for growing large zircon crystals. H_2O content influences not only crystal growth but also the nucleation and distribution of zircon in the charge. Sparse nucleation and relatively large zircon crystals occurred at high H_2O contents (>20 wt.% H_2O). In this case, gravity segregation usually occurred, leaving zircon crystals concentrated at the bottom of the charge within the capsule (Figure 2f1). In contrast, dense nucleation and tiny zircon crystals were randomly distributed throughout the charges at low H_2O contents (~10 wt.% H_2O; Figure 3a1). This observation is consistent with the experimental result that supercritical fluids with moderate H_2O contents have low viscosity (Audétat & Keppler, 2004).

Textures of quenched glasses generally show uniform appearance for individual run, but change with pressure, temperature, and bulk H_2O contents. They are variably vesiculated, varying from bubble poor (Figures 2a1 and 2a2) to bubble rich (Figures 2b1, 2b2, 2e1 and 2e2) with increasing bulk H_2O contents, but such trend becomes invalid when bulk H_2O contents are greater than 35 wt.%. In the H_2O-rich experiments, both large irregular vesicle and tiny round vesicle are present in glasses at 2.0 GPa and 900°C–1000°C (Figures 2c1, 2c2, 2d1, 2d2, 2f1 and 2f2). However, the density of tiny round vesicles nearly remains unchanged with increasing bulk H_2O content (Figures 2c2, 2d2 and 2f2). The formation of large irregular vesicles may result from the low viscosity of the H_2O-rich supercritical fluids, which improves the ability of the exsolved H_2O to migrate and coalesce during quenching. In contrast, these large irregular vesicles are not observed within the samples at 2.0 GPa, 800°C and 4.0–6.0 GPa, 1000°C (Figures 3a1–3b2 and 3a1–3e2). Another feature for H_2O-rich experiments at 2.0 GPa, 900°C–1000°C is a rind of bubble-free to bubble-poor glasses that are adjacent to capsule walls (Figures 2b1, 2b2, 2c1 and 2f1), which are also observed at 4.0 GPa, 1000°C (Figures 3c1, 3c2, 3d1 and 3d2). Such glass textures are very similar to those from $NaAlSi_3O_8$-H_2O supercritical fluid (Makhluf et al., 2020), which may reflect precipitation sequence on quenching of a single H_2O-rich liquid. At 6.0 GPa, the inner glasses seem to be vesiculated (Figure 3e1). However, the polished surface of quenched glasses is rather smooth without observable vesicles (Figure 3e2). Tiny vesicles (~1 μm) were observed in H_2O-rich experiments caused by H_2O exsolution upon quenching, during which the exsolved
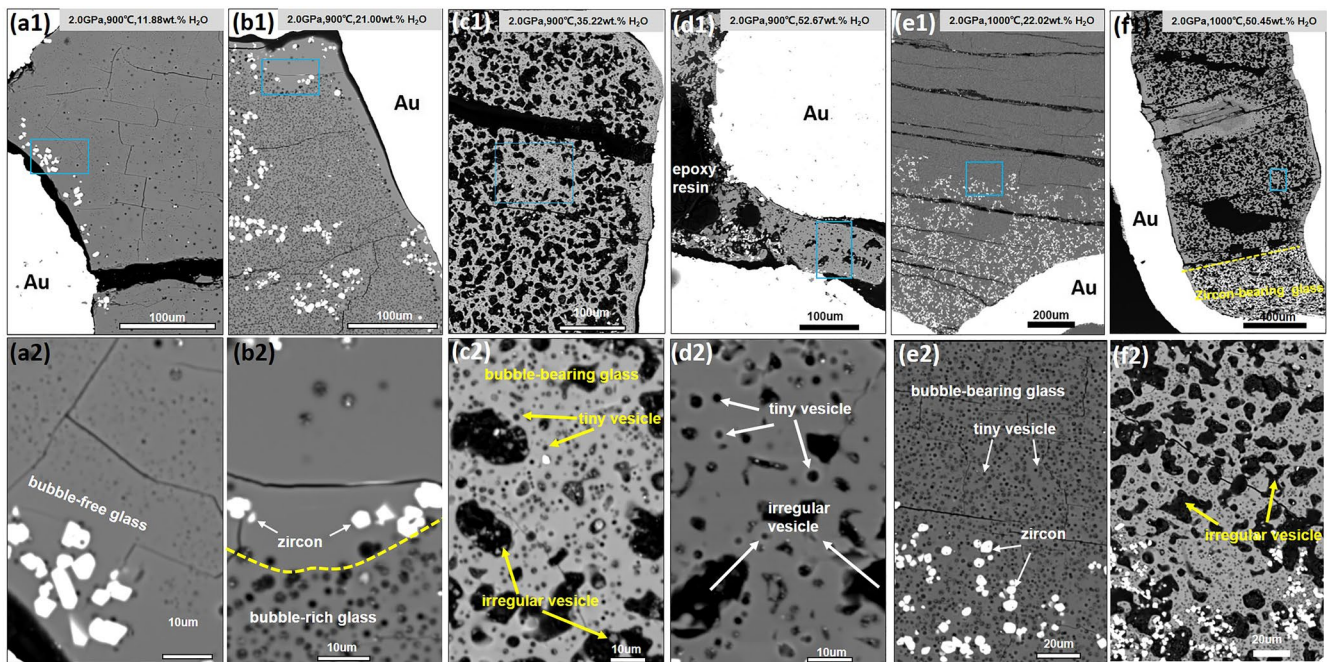
Figure 2. Back-scattered electron images of representative experimental run products at 2.0 GPa, 900°C–1000°C. (a1) Run AZ7: 2.0 GPa, 900°C, 11.88 wt.% H_2O. (a2) Magnification of the area marked by blue box in (a1). Zircon grains are subhedral to euhedral and glasses are bubble-poor to bubble-free. (b1) Run AZ8: 2.0 GPa, 900°C, 21.00 wt.% H_2O. (b2) Magnification of the area marked by blue box in (b1). Bubble poor glasses preferentially distribute along the capsule walls, whereas bubble-rich glasses fill the inner part of capsules. (c1) Run AZ8: 2.0 GPa, 900°C, 21.00 wt.% H_2O. (c2) Magnification of the area marked by blue box in (c1). Both irregular large vesicles and tiny vesicles are observed within glasses. (d1) Run AZ11: 2.0 GPa, 900°C, 52.67 wt.% H_2O. (d2) Magnification of the area marked by blue box in (d1). Irregular large vesicles coexist with tiny vesicles. (e1) Run AZ2: 2.0 GPa, 1,000°C, 22.02 wt.% H_2O. (e2) Magnification of the area marked by blue box in (e1). Tiny vesicles are homogeneously distributed within the glasses. (f1) Run AZ2: 2.0 GPa, 1000°C, 50.45 wt.% H_2O (f2).

H_2O separated from a hydrous melt (Hayden & Manning, 2011; Klimm et al., 2008; Makhluf et al., 2020). Quenched glassy globules and large round void spaces or tiny glass spheres were not found, indicating no coexistence of melt and aqueous fluid during the experiments (Kawamoto et al., 2012; Makhluf et al., 2020; Skora et al., 2015). These observations indicate that all the experiments were performed under supercritical conditions, consistent with the inference from phase relationships in the $KAlSi_3O_8$-H_2O system.

3.3. H_2O Contents in Quenched Glasses and High *P-T* Supercritical Fluids

As shown above, the tiny vesicles (typically ~1.0 μm) are dispersed throughout the quenched glasses in most cases. They represent quench H_2O exsolved from hydrous liquids during isobaric cooling, but are not caused by the immiscibility of the two phases during the experiment. Nearly all the quenched glasses underwent different degrees of H_2O exsolution, depending on the quenching rates and paths. As a result, the H_2O contents estimated in the quenched glasses (*H_2O in Table 1: obtained by the difference in the EPMA total of 100%) were nearly always lower than those expected in the supercritical fluid (**H_2O in Table 1: calculated from mass balance). What calls for special attention is that H_2O content (*H_2O in Table 1) calculated by the difference of anhydrous oxide totals from 100% represents the maximum H_2O concentration stored in quenched glasses. In the process of EMPA analysis, the analytical points were positioned over bubble-free (or bubble-poor) glasses as much as possible. However, the vesicles in some experiments are too abundant to allow the analysis of bubble-free glasses. In this case, the lower analytical totals would result in higher values of H_2O concentration estimated by difference and their potential uncertainties caused by tiny vesicles are hardly evaluated. Although absolute concentrations of oxides are underestimated because of tiny vesicles, element ratios are not significantly affected and thus give reliable H_2O contents in supercritical fluids (**H_2O in Table 1) based on mass balance calculation. It should be noted that significant H_2O loss through capsule walls during experiments was unlikely. Truckenbrodt and Johannes (1999) performed piston-cylinder experiments at 1.0 GPa and 900°C–1100°C to test the permeability of capsule materials Au,
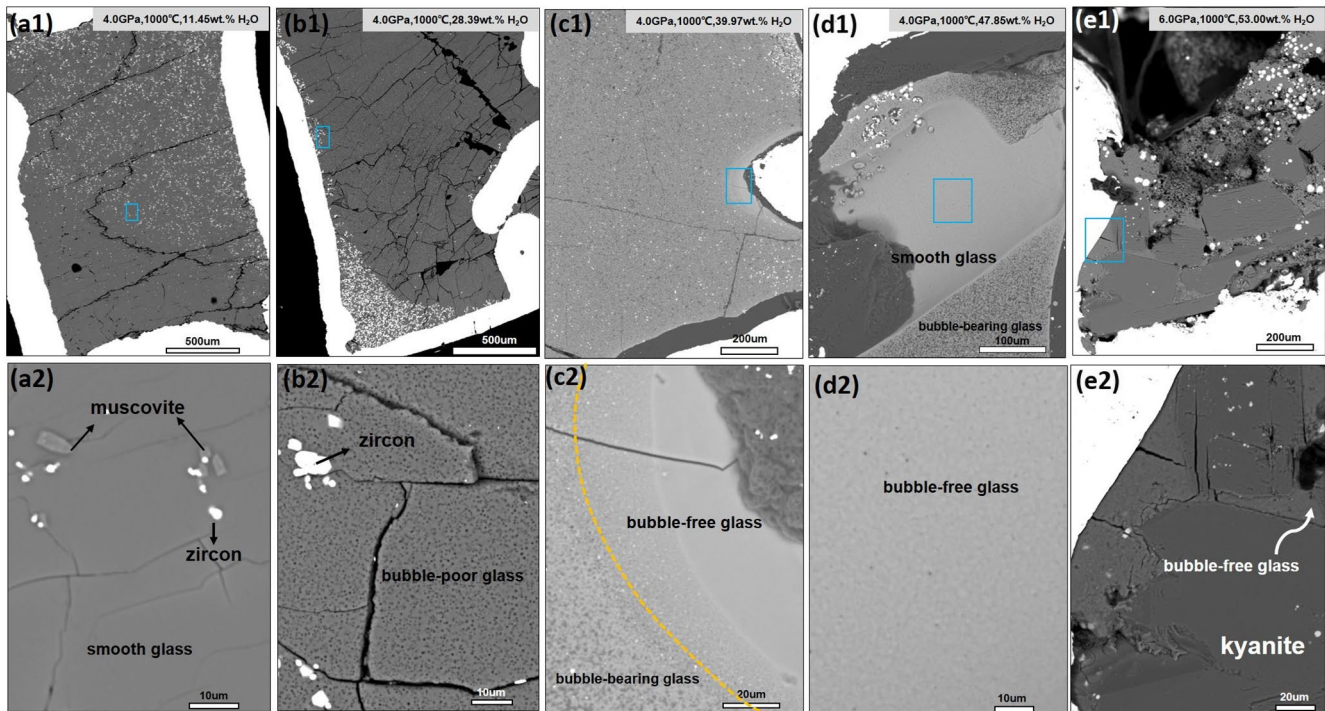
Figure 3. Back-scattered electron images of representative experimental run products at 4.0–6.0 GPa, 1000°C. (a1) Run AZ18: 4.0 GPa, 1000°C, 11.45 wt.% H_2O. Zircon crystals always distribute randomly through the capsule. (a2) Magnification of the area marked by blue box in panel (a1). Glasses are bubble-free and zircon and muscovite crystals are mostly subhedral. (b1) Run AZ20: 4.0 GPa, 1000°C, 28.39 wt.% H_2O. Zircon crystals are generally concentrated to the bottom of the capsule. (b2) Magnification of the area marked by blue box in panel (b1). Subhedral zircon crystals distribute within bubble-poor glasses. (c1) Run AZ21: 4.0 GPa, 1000°C, 39.97 wt.% H_2O. (c2) Magnification of the area marked by blue box in panel (c1). The bubble-free glasses distribute along the capsule, whereas the bubble-bearing glasses concentrate at the inner of capsule. (d1) Run AZ22: 4.0 GPa, 1000°C, 47.85 wt.% H_2O, showing coexistence of bubble-free glasses and bubble-bearing glasses. The bubble-free glasses and capsule walls are likely to be adjacent but the former detached from the sample during polishing. (d2) Magnification of the area marked by blue box in panel (d1). (e1) Run AZ26: 6.0 GPa, 1000°C, 53.00 wt.% H_2O. The bubble-free glasses are present, but significantly detached from the capsule during polishing. (e2) Magnification of the area marked by blue box in panel (e1). Euhedral kyanite crystals distribute within the bubble-free glasses.

$Ag_{75}Pd_{25}$, and Pt to pure H_2O and C-H-O fluids. Their results show that no detectable H_2O loss was observed in any capsule material at $T \leq 1050°C$, and this is confirmed by Makhluf et al. (2020). H_2O loss through capsule walls in the experiments in this study is thus less possible due to the lower run temperatures ($\leq 1000°C$). Moreover, zircon solubility in supercritical fluids varies regularly with H_2O content obtained from mass balance calculations (see Section 3.5), which indicates H_2O loss was not significant enough to obscure the primary result if it does occur. Therefore, H_2O contents (**H_2O in Table 1) calculated from the mass balance assuming a closed system are estimated to be more representative of the actual H_2O contents in supercritical fluids.

3.4. ZrO_2 Contents in Quenched Glasses and High P-T Supercritical Fluids

Since supercritical fluids underwent H_2O exsolution during quenching, ZrO_2 contents in the quenched glasses measured by the EPMA (column 13 in Table 2) should be corrected to their values in the supercritical fluids, which represent zircon solubility in supercritical fluids (column 12). According to the mass balance, we derived the following expression to calculate ZrO_2 content in a supercritical fluid:

$$X_{Zr} = \frac{X_{Zr}^{measured} \cdot \left(100 - ^{**} H_2O\right)}{Total^{measured}},$$

where X_{Zr} and **H_2O stand for ZrO_2 contents and H_2O concentrations in supercritical fluids, respectively, $X_{Zr}^{measured}$ and $Total^{measured}$ are ZrO_2 contents and totals of anhydrous oxides in quenched glasses measured by EPMA, respectively. Details about derivations of the above equation and the evaluation of potential effect of
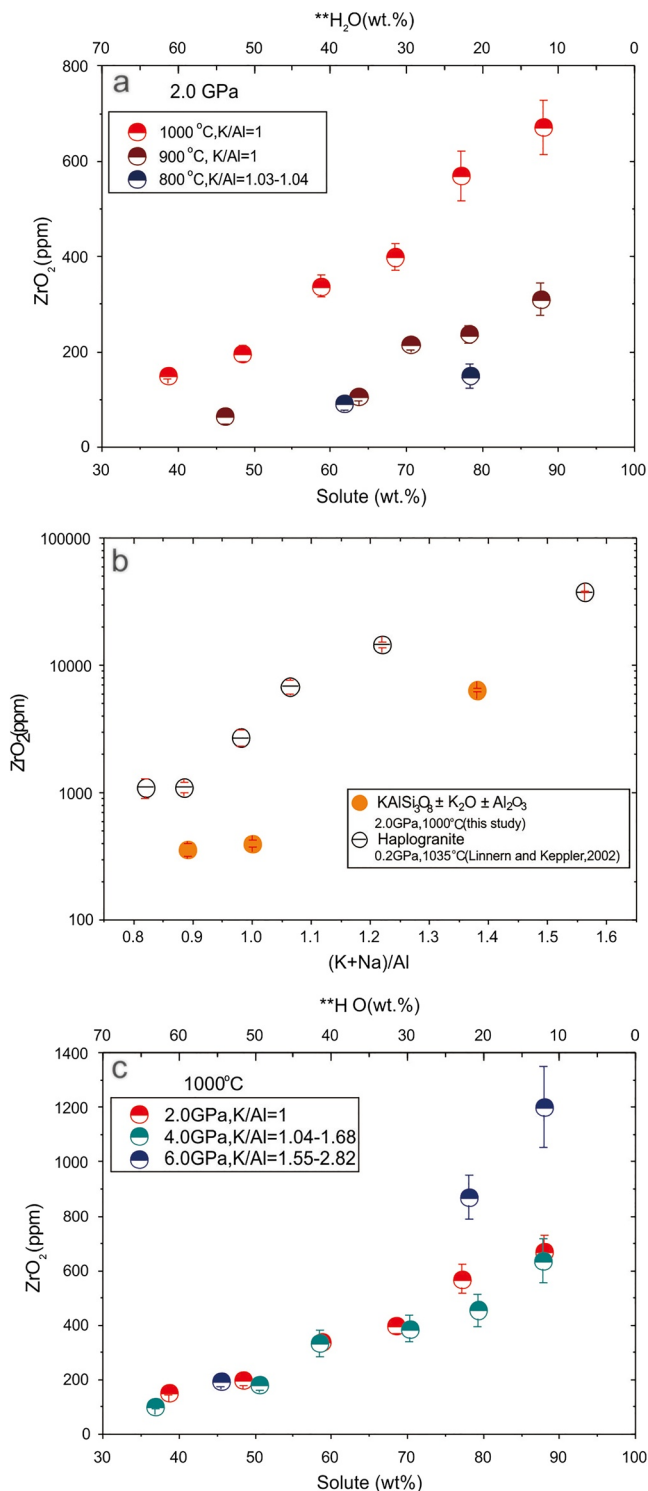
Figure 4. Zircon solubilities in solute-rich supercritical fluids. (a) Data for runs at 2.0 GPa and 800°C–1000°C; (b) variation of Zircon solubility with molar (K + Na)/Al ratio in supercritical fluids with the solubility data from the heplogranite-H_2O system (Linnen & Keppler, 2002) shown for comparison. (c) Comparison of the 1000°C data from 4.0 and 6.0 GPa runs with those from 2.0 GPa runs; Error bars represent σ standard deviation.

tiny vesicles within glasses on zircon solubility calculations in supercritical fluids are provided in Supporting Information S1.

Another major problem in all experimental studies of zircon solubility in a fluid is to assess attainment of equilibrium. In this study, all the experiments were run between 96 and 168 h, which is much longer than the time of 30 min required to reach the steady Zr concentration in aqueous fluids (e.g., Wilke et al., 2012). Kinetic experiments show that zircon dissolution in aqueous fluid can be fully equilibrated within 3 h at temperatures ≥300°C (C. Schmidt et al., 2006). High diffusion of zirconium is expected in supercritical fluids due to the high temperatures and low viscosity that are close to aqueous fluids (Audétat & Keppler, 2004). In this study, equilibrium was approached between zircon and the supercritical fluids, as indicated by the following lines of evidence: (a) the zircon crystals produced in all the runs are euhedral to subhedral; (b) the quenched glasses are homogenous with respect to Zr and other major elements; and (c) zircon solubility varies systematically as a function of H_2O, temperature and solute content and composition (see the section below). We are therefore confident that ZrO_2 contents in supercritical fluids here represent true chemical equilibrium values.

3.5. Zircon Solubility at Experimental Conditions

In the investigated *P-T* conditions and solute compositions, zircon solubility (expressed as ZrO_2 content at zircon saturation) in the supercritical fluid ranges from 65 to 6,367 ppm (Table 2). The solubility data are plotted in Figure 4a–4c, and the effects of *T, P*, solute content (H_2O content), and solute alkalinity (K/Al) are addressed as follows.

Figure 4a shows the results in the $KAlSi_3O_8$-H_2O system at 2.0 GPa and 800°C–1000°C with solute contents in the range of 37–88 wt.% (12–63 wt.% H_2O). The experiments at 900°C and 1000°C only produced zircon + supercritical fluid. The data from these experiments thus allow the direct evaluation of the effects of temperature and solute content on solubility. At 900°C, zircon solubility increases linearly from 65 to 310 ppm when the solute content increases from ∼45 to ∼88 wt.%; at 1.000°C, zircon solubility linearly increases from 151 to 671 ppm with increasing solute content from ∼37 to ∼88 wt.%. At a given solute content, the zircon solubility at 1000°C is ∼200–300 ppm higher than that at 900°C. The positive effects of solute content and temperature are in agreement with the experimental results with aqueous fluids (e.g., Bernini et al., 2013; Wilke et al., 2012). At 800°C, the results from the two runs are only slightly lower than those at 900°C with similar solute contents. This is because the solute K/Al ratios in these two runs were elevated due to the crystallization of muscovite (see below for the effect of alkalinity). High solute contents (>50 wt.%) result in zircon solubility of >100 ppm at 2.0 GPa and 800°C–1000°C, suggesting that solute-rich supercritical fluids are very effective agents for the transfer of Zr.

Figure 4b shows the results in the $KAlSi_3O_8$ + K_2O or Al_2O_3 – H_2O systems at 2.0 GPa, 1000°C, and ∼30 wt.% H_2O, including three runs, AK2, AZ3, and AK1, with solute molar K/Al ratios (Table 2) of 0.90, 1.0, and 1.38, respectively. Zircon solubility in AK2 (356 ± 40 ppm) is only slightly lower than that (399 ± 28 ppm) in AZ3, indicating that slight peraluminous solute does not cause a significant change in zircon solubility. In contrast, zircon solubility (6,367 ppm) in AK1 is more than 10 times higher
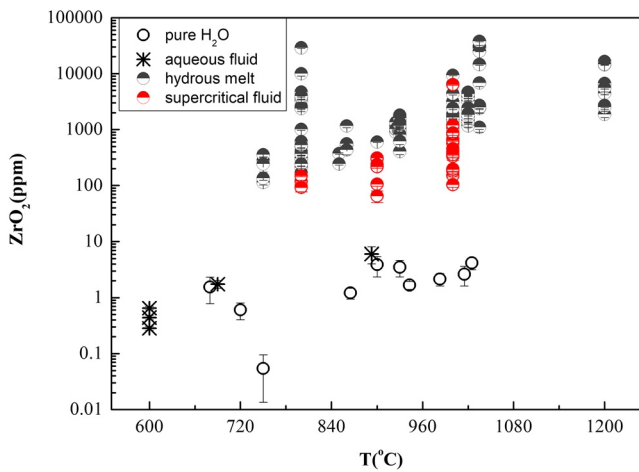
Figure 5. Comparison of zircon solubility in solute-rich supercritical fluids (this study) to the literature data in dilute aqueous fluids (including pure H_2O fluid) and hydrous melts. Zircon solubilities in hydrous melts are 2–3 orders of magnitude higher than those in dilute aqueous fluids. In solute-rich supercritical fluids, zircon solubilities are 1–2 orders of magnitude higher than those in dilute aqueous fluids, closer to those in the hydrous melts. Data sources: pure H_2O fluid and aqueous fluid from Bernini et al. (2013) and Ayers et al. (2012); hydrous melts from Linnen and Keppler (2002), Boehnke et al. (2013), Linnen (2005), Aseri et al. (2015), Rubatto and Hermann (2007), Gervasoni et al. (2016), and Watson & Harrison, 1983; supercritical fluid from this study.

than that in AZ3, indicating that the addition of K_2O to the $KAlSi_3O_8$-H_2O system strongly enhances zircon solubility. The strong increase in zircon solubility with solute alkalinity observed in this study is consistent with previous studies on zircon solubility in hydrous melts (e.g., Linnen & Keppler, 2002) and solute-rich fluids (Wilke et al., 2012).

Figure 4c compares the results from 4.0 and 6.0 GPa with those from 2.0 GPa in the $KAlSi_3O_8$-H_2O system at 1000°C. The pressure dependence of zircon solubility in the $KAlSi_3O_8$-H_2O system should be similar to that of TiO_2 solubility in the $NaAlSi_3O_8$-H_2O system (Hayden & Manning, 2011) and SiO_2-H_2O system (Chen et al., 2018); that is, pressure should result in a decrease in zircon solubility in solute-rich fluids (Wilke et al., 2012). However, zircon solubilities at 4.0 GPa show overlap with those at 2.0 GPa, although the former is generally slightly lower than the latter at a similar solute content. This is because crystallization of Al-rich phases muscovite or kyanite at 4.0 GPa results in solute K/Al ratios (1.05–1.68) that are higher than 1.0, and the negative effect of pressure on zircon solubility is offset by the positive effect of the solute K/Al ratio. At 6.0 GPa, crystallization of kyanite strongly elevates the solute K/Al ratio (from 1.0 to 1.55–2.82), leading to the solubility reversing to values higher than those at 2.0 GPa. Therefore, kyanite crystallization results in strongly peralkaline fluids and the highest zircon solubility in the $KAlSi_3O_8$-H_2O system. Kyanite crystallization profoundly influences the solute alkali/Al ratio and thus the zircon solubility and element carrying capacity of fluids during deep subduction.

4. Discussion

4.1. Effect of Complexation on Zircon Solubility in Supercritical Fluids

Zircon solubility has been widely investigated in both dilute aqueous fluids and hydrous melts with a variety of compositions. The first study on zircon solubility in pure H_2O and dilute aqueous fluids was Ayers and Watson (1991), who employed a weight-loss method to measure the solubility at 1.0–3.0 GPa and 800°C–1200°C. They reported ZrO_2 contents in fluids in equilibrium with zircon and quartz reaching 1,800 ppm. However, as pointed out by Tropper and Manning (2005), Ayers and Watson (1991) used a large capsule design, which had a large temperature gradient. Transport and reprecipitation of zircon affect all of their results, leading to significantly overestimated solubility. More careful experiments performed later by Ayers et al. (2012) show that zircon solubility in similar fluids is nearly 300 times lower. The much lower solubility in dilute aqueous fluids is supported by in situ observation of dissolving zircon grains in HDAC, which give a maximum solubility of 6 ppm in the fluids with <5 wt.% solutes at conditions reaching 2.0 GPa and 1025°C (Bernini et al., 2013). More solute-rich fluids (10–30 wt.% solutes) in $Na_2Si_3O_7$-H_2O, $Na_2Si_3O_7$+Al_2O_3-H_2O, $Na_2Si_2O_5$-H_2O, and $NaAlSi_3O_8$-H_2O systems demonstrated that zircon solubility increases with temperature, solute content, and Na/Al ratio but decreases with pressure (Wilke et al., 2012). These solute-rich fluids show much higher zircon solubility (20–600 ppm) than dilute aqueous fluids, although these fluids are Al-free or Al-low and may not represent natural compositions. In contrast, zircon solubility shows large variability in hydrous melts over a wide range of aluminous to alkaline silicate compositions and greatly increases in more alkali-rich and depolymerized melts (Boehnke et al., 2013; Gervasoni et al., 2016; Linnen, 2005; Linnen & Keppler, 2002; Watson & Harrison, 1983). Figure 5 gives a comparison of our experimental data of zircon solubility in solute-rich supercritical fluids to literature data of that in dilute aqueous fluids (including pure H_2O fluid) and hydrous melts. Zircon solubility in hydrous melts is 2–3 orders of magnitude higher than that in dilute aqueous fluids. In solute-rich supercritical fluids, zircon solubility is 1–2 orders of magnitude higher than that in dilute aqueous fluids and closer to those in hydrous melts. The systematic variations of zircon solubility with solute content and composition in liquids could be explained by the complexation mechanism for Zr.

Zirconium is expected to exist as Zr (IV) in fluids and melts because only the quadrivalent oxidation state is stable over a wide range of redox conditions (Aja et al., 1995). Zr^{4+} speciation is dominated by eight-fold-coordinated hydrated complexes in pure H_2O and dilute aqueous fluids (Adair et al., 1997; Ayers & Watson, 1991; Ayers et al., 2012; Louvel et al., 2013). In this case, zircon solubility may vary with pH in high-pressure aqueous fluids (Ayers & Watson, 1991). In contrast, the investigations by X-ray absorption spectroscopy found that six-coordinated alkali-zircon silicate clusters dominate Zr speciation in solute-rich fluids (Louvel et al., 2013; Wilke et al., 2012). Considering the similar behavior of Na and K in fluids and melts (Mysen & Armstrong, 2002), we speculate that Zr is incorporated into the $KAlSi_3O_8$-H_2O fluids, probably as Zr-O-Si/K clusters, similar to the Zr-O-Si/Na polymeric species in Na-Al-silicate fluids (Louvel et al., 2013). In this case, fluids pH should have minor or negligible effect on zircon solubility. In situ Raman spectra in the HDAC experiments show that most silicate species are present as dimers and trimers in $KAlSi_3O_8$-H_2O supercritical fluids (Mibe et al., 2008). The strong enhancement of zircon solubility with $KAlSi_3O_8$ contents and K/Al ratios in supercritical fluids in our experiments is thus attributed to the formation of alkali (K) zircono-silicate complexes.

4.2. Formation of Solute-Rich and High-Alkali/Al Fluids

The efficiency of fluid-driven chemical transfer in subduction zones will depend on *P-T* conditions and composition of slab-derived fluids. Fluids are continuously released through the metamorphic dehydration sediments, altered oceanic crust, and serpentinized lithosphere when a slab travels along the prograde *P-T* path during subduction (Schmidt & Poli, 2014). These fluids could reach temperatures in the range of 700°C–900°C at sub-arc depths (∼80–180 km or ∼2.0–6.0 GPa) (Cooper et al., 2012; Syracuse & Abers, 2006) and may dissolve significant amounts of silica, alkalis, and alumina to form solute-rich supercritical fluids when infiltrating overlying sediments and the altered oceanic crust. The multiphase fluid inclusions in exhumed eclogites are considered as natural evidence for the presence of solute-rich supercritical fluids under high-pressure to ultrahigh-pressure conditions (Ferrando et al., 2005; Hermann et al., 2013; Zhang et al., 2008; Zheng & Hermann, 2014). Therefore, supercritical fluids derived from subducting slabs may be pervasive within the sub-arc depths.

Zircon and rutile solubility are extremely low in dilute aqueous fluids (<10 wt.% solutes) and should hence be considered inefficient agent of transfer of HFSE. In comparison, supercritical fluids and hydrous melts will be more efficient in transferring HFSEs out of the slab, as suggested both by our new results and previous studies (Kessel et al., 2005; Ni et al., 2017; but also Antignano & Manning, 2008 or Wilke et al., 2012). A comparison with literature data (Figure 5 in this study and Figure 3 in Chen et al., 2018) shows that the solubilities of zircon and rutile in solute-rich supercritical fluids are 1–2 orders of magnitude higher than those in dilute aqueous fluids. In particular, the solubilities of these two minerals increase with temperature, solute content, and alkalinity. These factors profoundly influence the dissolution behavior of HFSEs. Although the positive temperature effect could be partly offset by the negative pressure effect, the increase in solute content, particularly alkalinity (alkali/Al), with slabs traveling into the deep mantle may strongly enhance zircon and rutile solubilities. Our experiments in the simplified $KAlSi_3O_8$-H_2O system at 2.0–6.0 GPa show that crystallization of Al-rich minerals kyanite and muscovite leads to K/Al > 1.0 in the coexisting supercritical fluids. In particular, kyanite contains 62 wt.% Al_2O_3, which strongly elevates the alkali/Al ratio in the coexisting fluid. The experiments of Hermann and Spandler (2008) that use subducted pelites as starting materials also show that hydrous melts become more alkali-rich with increasing kyanite crystallization, with the ASI (alumina saturation index, Al/(Na + K + 2Ca)) varying from 1.12 and 0.86 to 0.63 when the pressure changes from 2.5 and 3.5 to 4.5 GPa at 800°C. Thermodynamic calculations also demonstrated an increase of fluid alkalinity with slab subducted depths (Galvez et al., 2016). Therefore, as a plate migrates into the deep mantle, the solute content and alkali/Al ratio in the derived fluids increases, potentially leading to significant enhancement of HFSEs dissolution and transport.

4.3. Zirconium Transfer in Subduction Zones

Zirconium could be efficiently extracted from subducted crust rocks by solute-rich supercritical fluids, as evidenced by newly formed zircon in orogenic peridotites at slab-mantle interface (Faithfull et al., 2018; Li
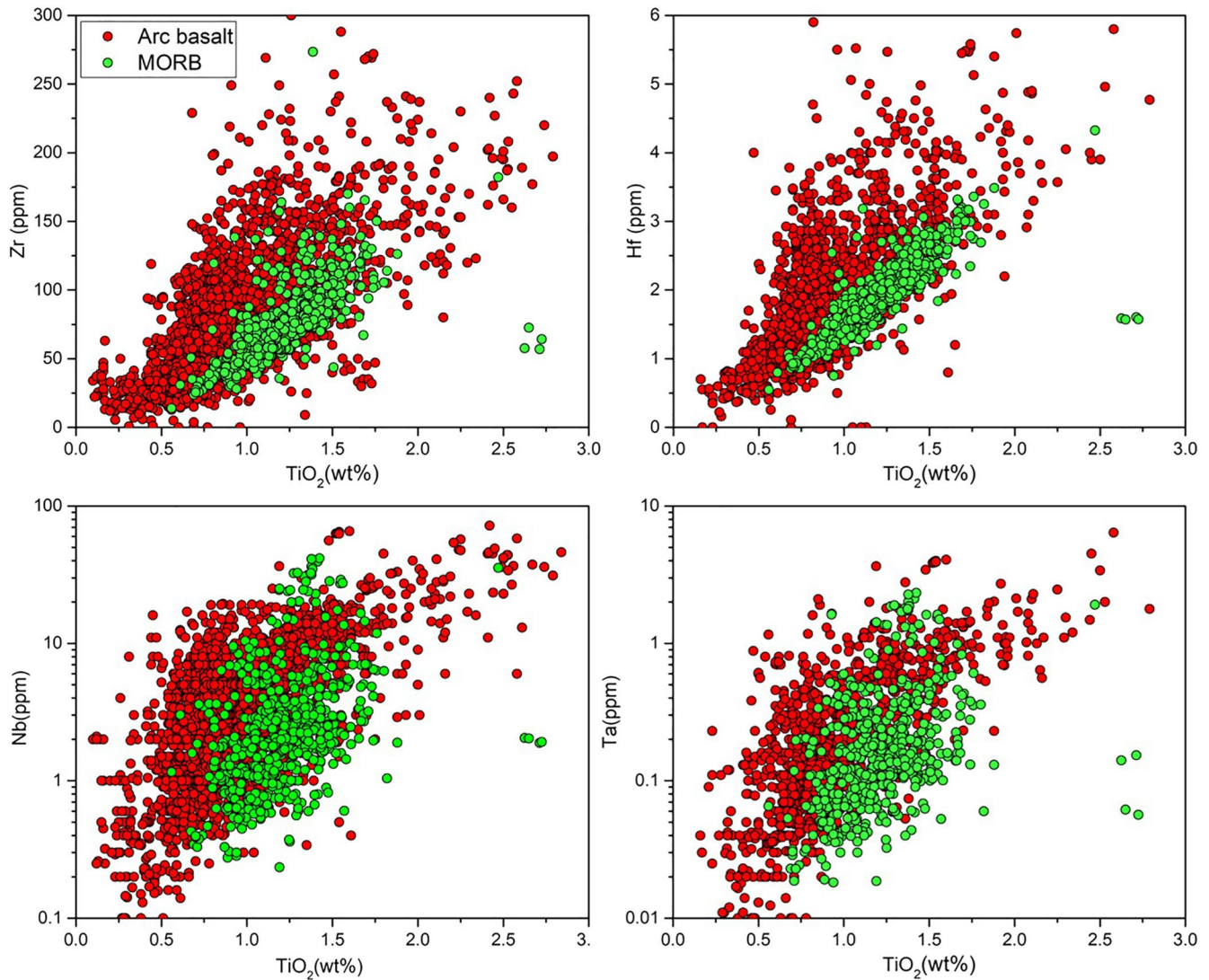
Figure 6. Zr, Hf, Nb, Ta versus TiO$_2$ for global primitive arc basalts and mid-ocean ridge basalts (MORBs). TiO$_2$ was used as a proxy of the mantle melting degree. The primitive arc basalts are apparently higher in Zr and Hf, and to a lesser degree in Nb and Ta, than MORBs, indicating that arc magma source regions are more or less enriched by the input of slab-derived, HFSE-rich components. Data sources for the primitive MORBs from Jenner and O'Neill (2012), Gale et al. (2013), and Shimizu et al. (2016), and for the primitive arc basalts from http://georoc.mpch-mainz.gwdg.de/georoc/. To minimize crystal fractionation, crustal assimilation, magma mixing, and crystal accumulation, the data are filtered by the following criteria: MgO >8.0 wt.%, Mg# = 60–75, and Ni > 100 ppm. The data on this figure are provided in Table S1.

et al., 2016). However, the question arises as to whether or not zirconium can be transferred to the source of arc magma or to the volcanic arc. Arc magmas, compared to MORBs, have a characteristic of depletion in HFSEs (Zr, Hf, Nb, and Ta) relative to LILEs. However, this does not mean that fluids cannot mobilize these elements into the mantle wedge. We here use TiO$_2$ as the proxy of mantle melting degree to compare the absolute concentrations of Zr, Hf, Nb, and Ta between global primitive arc basalts and MORBs (data sources and filtration criteria are given below Figure 6). The depleted mantle (MORB source) has 0.11 wt.% TiO$_2$, 5.1 ppm Zr, 0.16 ppm Hf, 0.15 ppm Nb, and 0.01 ppm Ta (Workman & Hart, 2005). The high Ti contents (relative to Nb, Ta, Zr, and Hf) in the mantle make Ti insensitive in reflecting the Ti mobility from slab to wedge. In addition, Ti is highly incompatible with mantle minerals (Wang et al., 2019). TiO$_2$ contents are therefore an excellent proxy for the melting degree of the mantle wedge (Kelley et al., 2006; Schmidt & Jagoutz, 2017). Figure 6 clearly shows that primitive arc basalts generally have higher Zr and Hf concentrations and, to a lesser extent, Nb and Ta contents than those in MORBs at a given melting degree (TiO$_2$), indicating that Zr, Hf, Nb, and Ta in the arc magma source regions are enriched more or less by the input of slab-derived components.

Aqueous fluid is too dilute to enrich arc magma mantle source regions in zirconium (Bernini et al., 2013), whereas solute-rich supercritical fluid is expected to be an ideal agent for the mobilization of Zr in subduction zones. It is worth noting that mass transfer mediated by supercritical fluid in subduction zones is more likely to occur in steps (Manning, 2004). While supercritical fluids may be initial agents for leaching elements from the slab, they are likely to separate into immiscible hydrous melts and aqueous fluids at the slab-mantle interface in response to changes in pressure, temperature, and especially bulk rock compositions (Chen et al., 2018; Manning, 2004). As the process continues, hydrous melts will react with mantle peridotites to form metasomatic domains containing zircon (e.g., Faithfull et al., 2018; Kalfoun et al., 2002; Li et al., 2016; Malaspina et al., 2006), whereas aqueous fluids may ascend to the arc magma source regions (Malaspina et al., 2006). In this case, zirconium mobilization is controlled not only by zircon solubility in supercritical fluids but also by partitioning of Zr between hydrous melts and aqueous fluids. The high partition coefficient of Zr between aqueous fluid and hydrous melt ($D_{\text{fluid/melt}}^{\text{Zr}} = 0.30 \pm 0.10$, Louvel et al., 2014) implies ca. 23% of zirconium dissolved in supercritical fluids would be assigned to aqueous fluids and transported to the arc magma source regions.

HFSEs are hence transportable from subducting slab to mantle wedge, but the characteristic HFSEs depletion recorded in arc magmas may partly result from fluid-rock interactions at the slab-mantle interface, during which most HFSEs were scavenged by newly formed zircon and rutile (Faithfull et al., 2018; Kalfoun et al., 2002; Li et al., 2016). Such a depletion may indicate a lower solubility of HFSEs relative to LILEs but does not necessarily mean immobility of these elements in subduction-zone fluids.

5. Conclusions

Zircon solubility in supercritical $KAlS_3O_8$-H_2O fluids increases linearly with solute content. The addition of K_2O to this system or crystallization of peraluminous phases kyanite and muscovite at high pressures strongly enhance the solute alkalinity (alkali/Al) and zircon solubility. These results confirm that the formation of alkali-Zr-silicate polymeric species (Louvel et al., 2013; Wilke et al., 2012) is the fundamental incorporation mechanism of Zr in solute-rich fluids. Comparison with published data indicates that zircon solubility in solute-rich supercritical fluids is 1–2 orders of magnitude higher than that in dilute aqueous fluids. Solute-rich supercritical fluids, particularly those with peralkaline compositions, are thus effective agents for the transfer of Zr and other HFSEs in subduction zones.

As the slab descends and pressure and temperature increase, the fluids released from the subducting slab are expected to become more solute-rich. In particular, the formation of Al-rich phases kyanite and muscovite result in alkali/Al ratios that are much greater than unity in the derived fluids, largely enhancing HFSE solubility in the fluids. Therefore, the capability of solute-rich supercritical fluids in dissolving and transporting HFSEs significantly increases with subduction depth. The high zircon solubility in solute-rich supercritical fluids explains not only the dissolution and re-precipitation of zircon in metamorphic rocks but also the significant transfer of HFSEs from slab to wedge.

Data Availability Statement

Table S1 is stored in Zendo and can be download online (https://zenodo.org/record/5336476).

References

Adair, J. H., Karup, H. G., Venigalla, S., & Tsukada, T. (1997). A review of the aqueous chemistry of the zirconium-water system to 200°C. *Materials Research Society Symposium Proceedings*, *432*, 101–112. https://doi.org/10.1557/proc-432-101

Aja, S. U., Wood, S. A., & Williams-Jones, A. E. (1995). The aqueous geochemistry of Zr and the solubility of some Zr-bearing minerals. *Applied Geochemistry*, *10*, 603–620. https://doi.org/10.1016/0883-2927(95)00026-7

Antignano, A., & Manning, C. E. (2008). Rutile solubility in H_2O, H_2O-SiO_2, and H_2O-$NaAlSi_3O_8$ fluids at 0.7–2.0 GPa and 700–1000°C: Implications for mobility of nominally insoluble elements. *Chemical Geology*, *255*, 283–293. https://doi.org/10.1016/j.chemgeo.2008.07.001

Aseri, A. A., Linnen, R. L., Che, X. D., Thibault, Y., & Holtz, F. (2015). Effects of fluorine on the solubilities of Nb, Ta, Zr and Hf minerals in highly fluxed water-saturated haplogranitic melts. *Ore Geology Reviews*, *64*, 736–746.

Audétat, A., & Keppler, H. (2004). Viscosity of fluids in subduction zones. *Science*, *303*, 513–516. https://doi.org/10.1126/science.1092282

Audétat, A., & Keppler, H. (2005). Solubility of rutile in subduction zone fluids, as determined by experiments in the hydrothermal diamond anvil cell. *Earth and Planetary Science Letters*, *232*, 393–402. https://doi.org/10.1016/j.epsl.2005.01.028

Ayers, J. C., & Watson, E. B. (1991). Solubility of apatite, monazite, zircon, and rutile in supercritical aqueous fluids with implications for subduction zone geochemistry. *Philosophical Transactions: Physical Sciences and Engineering*, *335*, 365–375. https://doi.org/10.1098/rsta.1991.0052

Ayers, J. C., Zhang, L., Luo, Y., & Peters, T. J. (2012). Zircon solubility in alkaline aqueous fluids at upper crustal conditions. *Geochimica et Cosmochimica Acta*, *96*, 18–28. https://doi.org/10.1016/j.gca.2012.08.027

Bernini, D., Audétat, A., Dolejš, D., & Keppler, H. (2013). Zircon solubility in aqueous fluids at high temperatures and pressures. *Geochimica et Cosmochimica Acta*, *119*, 178–187. https://doi.org/10.1016/j.gca.2013.05.018

Boehnke, P., Watson, E. B., Trail, D., Harrison, T. M., & Schmitt, A. K. (2013). Zircon saturation re-revisited. *Chemical Geology*, *351*, 324–334. https://doi.org/10.1016/j.chemgeo.2013.05.028

Borisov, & Aranovich (2019). Zircon solubility in silicate melts: New experiments and probability of zircon crystallization in deeply evolved basic melts. *Chemical Geology*, *510*, 103–112. https://doi.org/10.1016/j.chemgeo.2019.02.019

Bureau, H., & Keppler, H. (1999). Complete miscibility between silicate melts and hydrous fluids in the upper mantle: Experimental evidence and geochemical implications. *Earth and Planetary Science Letters*, *165*, 187–196. https://doi.org/10.1016/S0012-821X(98)00266-0

Chen, W., Xiong, X., Wang, J., Xue, S., Li, L., Liu, X., et al. (2018). TiO_2 solubility and Nb and Ta partitioning in Rutile-Silica-Rich supercritical fluid systems: Implications for Subduction Zone Processes. *Journal of Geophysical Research: Solid Earth*, *123*, 4765–4782. https://doi.org/10.1029/2018JB015808

Chen, W., Zhang, G., Ruan, M., Wang, S., & Xiong, X. (2021). Genesis of intermediate and silicic arc magmas constrained by Nb/Ta fractionation. *Journal of Geophysical Research: Solid Earth*, *126*, e2020JB020708. https://doi.org/10.1029/2020JB020708

Cooper, L. B., Ruscitto, D. M., Plank, T., Wallace, P. J., Syracuse, E. M., & Manning, C. E. (2012). Global variations in H_2O/Ce: 1. Slab surface temperatures beneath volcanic arcs. *Geochemistry, Geophysics, Geosystems*, *13*, 3. https://doi.org/10.1029/2011GC003902

Faithfull, J. W., Dempster, T. J., MacDonald, J. M., & Reilly, M., & EIMF. (2018). Metasomatism and the crystallization of zircon megacrysts in Archean peridotites from the Lewisian complex, NW Scotland. *Contributions to Mineralogy and Petrology*, *173*, 99. https://doi.org/10.1007/s00410-018-1527-5

Ferrando, S., Frezzotti, M. L., Dallai, L., & Compagnoni, R. (2005). Multiphase solid inclusions in UHP rocks (Su-Lu, China): Remnants of supercritical silicate-rich aqueous fluids released during continental subduction. *Chemical Geology*, *223*, 68–81. https://doi.org/10.1016/j.chemgeo.2005.01.029

Gale, A., Dalton, C. A., Langmuir, C. H., Su, Y., & Jean-Guy, S. (2013). The mean composition of ocean ridge basalts. *Geochemistry, Geophysics, Geosystems*, *14*(3), 489–518. https://doi.org/10.1029/2012GC004334

Galvez, M., Connolly, J., & Manning, C. (2016). Implications for metal and volatile cycles from the pH of subduction zone fluids. *Nature*, *539*, 420–424. https://doi.org/10.1038/nature20103

Gao, J., John, T., Klemd, R., & Xiong, X. (2007). Mobilization of Ti-Nb-Ta during subduction: Evidence from rutile-bearing dehydration segregations and veins hosted in eclogite, Tianshan, NW China. *Geochimica et Cosmochimica Acta*, *71*, 4974–4996. https://doi.org/10.1016/j.gca.2007.07.027

Gervasoni, F., Klemme, S., Rocha-Júnior, E. R. V., & Berndt, J. (2016). Zircon saturation in silicate melts: A new and improved model for aluminous and alkaline melts. *Contributions to Mineralogy and Petrology*, *171*, 21. https://doi.org/10.1007/s00410-016-1227-y

Hayden, L. A., & Manning, C. E. (2011). Rutile solubility in supercritical $NaAlSi_3O_8$-H_2O fluids. *Chemical Geology*, *284*, 74–81. https://doi.org/10.1016/j.chemgeo.2011.02.008

Hermann, J., & Rubatto, D. (2009). Accessory phase control on the trace element signature of sediment melts in subduction zones. *Chemical Geology*, *265*, 512–526. https://doi.org/10.1016/j.chemgeo.2009.05.018

Hermann, J., & Spandler, C. J. (2008). Sediment melts at sub-arc depths: An experimental study. *Journal of Petrology*, *49*, 717–740. https://doi.org/10.1093/petrology/egm073

Hermann, J., Zheng, Y. F., & Rubatto, D. (2013). Deep fluids in subducted continental crust. *Elements*, *9*, 281–287. https://doi.org/10.2113/gselements.9.4.281

Jenner, F. E., & O'Neill, H. S. C. (2012). Analysis of 60 elements in 616 ocean floor basaltic glasses. *Geochemistry, Geophysics, Geosystems*, *13*, Q02005. https://doi.org/10.1029/2011GC004009

Kalfoun, F., Ionov, D., & Merlet, C. (2002). HFSE residence and Nb/Ta ratios in metasomatised, rutile-bearing mantle peridotites. *Earth and Planetary Science Letters*, *199*, 49–65. https://doi.org/10.1016/S0012-821X(02)00555-1

Kawamoto, T., Kanzaki, M., Mibe, K., Matsukage, K. N., & Ono, S. (2012). Separation of supercritical slab-fluids to form aqueous fluid and melt components in subduction zone magmatism. *Proceedings of the National Academy of Sciences of the United States of America*, *109*, 18695–18700. https://doi.org/10.1073/pnas.1207687109

Kelley, K. A., Plank, T., Grove, T. L., Stolper, E. M., Newman, S., & Hauri, E. (2006). Mantle melting as a function of water content beneath back-arc basins. *Journal of Geophysical Research Solid Earth*, *111*(B9). https://doi.org/10.1029/2005JB003732

Kessel, R., Schmidt, M. W., Ulmer, P., & Pettke, T. (2005). Trace element signature of subduction-zone fluids, melts and supercritical liquids at 120–180 km depth. *Nature*, *437*, 724–727. https://doi.org/10.1038/nature03971

Klimm, K., Blundy, J. D., & Green, T. H. (2008). Trace element partitioning and accessory phase saturation during H_2O-saturated melting of basalt with implications for subduction zone chemical fluxes. *Journal of Petrology*, *49*(3), 523–553. https://doi.org/10.1093/petrology/egn001

Li, H.-Y., Chen, R.-X., Zheng, Y.-F., & Hu, Z. (2016). The crust-mantle interaction in continental subduction channels: Zircon evidence from orogenic peridotite in the Sulu orogen. *Journal of Geophysical Research: Solid Earth*, *121*, 687–712. https://doi.org/10.1002/2015JB012231

Li, W. C. & Ni, H. W. (2020). Dehydration at subduction zones and the geochemistry of slab fluids. *Science. China Earth Science*, *63*, 1925–1937. https://doi.org/10.1007/s11430-019-9655-1

Linnen, R. L. (2005). The effect of water on accessory phase solubility in subaluminous and peralkaline granitic melts. *Lithos*, *80*, 267–280.

Linnen, R. L., & Keppler, H. (2002). Melt composition control of Zr/Hf fractionation in magmatic processes. *Geochimica et Cosmochimica Acta*, *66*, 3293–3301. https://doi.org/10.1016/S0016-7037(02)00924-9

Louvel, M., Sanchen-Valle, C., Malfait, W. J., Cardon, H., Testemale, D., & Hazemann, J.-L. (2014). Constraints on the mobilization of Zr in magmatic-hydrothermal processes in subduction zones from in situ fluid-melt partitioning experiments. *American Mineralogist*, *99*, 1616–1625. https://doi.org/10.1016/j.lithos.2004.04.060

Louvel, M., Sanchez-Valle, C., Malfait, W. J., Testemale, D., & Hazemann, J.-L. (2013). Zr complexation in high pressure fluids and silicate melts and implications for the mobilization of HFSE in subduction zones. *Geochimica et Cosmochimica Acta*, *104*, 281–299. https://doi.org/10.1016/j.gca.2012.11.001

Makhluf, A. R., Newton, R. C., & Manning, C. E. (2020). Experimental investigation of phase relations in the system $NaAlSi_3O_8$-H_2O at high temperatures and pressures: Liquidus relations, liquid-vapor mixing, and critical phenomena at deep crust-upper mantle conditions. *Contributions to Mineralogy and Petrology*, *175*(8), 1–20. https://doi.org/10.1007/s00410-020-01711-2

Malaspina, N., Hermann, J., Scambelluri, M., & Compagnoni, R. (2006). Polyphase inclusions in garnet-orthopyroxenite (Dabie Shan, China) as monitors for metasomatism and fluid-related trace element transfer in subduction zone peridotite. *Earth and Planetary Science Letters*, *249*, 173–187. https://doi.org/10.1016/j.epsl.2006.07.017

Manning, C. E. (2004). The chemistry of subduction-zone fluids. *Earth and Planetary Science Letters*, *223*, 1–16. https://doi.org/10.1016/j.epsl.2004.04.030

Mibe, K., Chou, I.-M., & Bassett, W. A. (2008). In situ Raman spectroscopic investigation of the structure of subduction-zone fluids. *Journal of Geophysical Research: Solid Earth*, *113*, B4. https://doi.org/10.1029/2007JB005179

Mysen, B. O., & Armstrong, L. (2002). Solubility behavior of alkali aluminosilicate components in aqueous fluids and silicate melts at high pressure and temperature. *Geochimica et Cosmochimica Acta*, *66*, 2287–2297. https://doi.org/10.1016/S0016-7037(01)00824-9

Ni, H., Zhang, L., Xiong, X., Mao, Z., & Wang, J. (2017). Supercritical fluids at subduction zones: Evidence, formation condition, and physicochemical properties. *Earth-Science Reviews*, *167*, 62–71. https://doi.org/10.1016/j.earscirev.2017.02.006

Rubatto, D., & Hermann, J. (2003). Zircon formation during fluid circulation in eclogites (Monviso, Western Alps): Implications for Zr and Hf budget in subduction zones. *Geochimica et Cosmochimica Acta*, *67*, 2173–2187. https://doi.org/10.1016/S0016-7037(02)01321-2

Rubatto, D., & Hermann, J. (2007). Experimental zircon/melt and zircon/garnet trace element partitioning and implications for the geochronology of crustal rocks. *Chemical Geology*, *241*(1-2), 38–61. https://doi.org/10.1016/j.chemgeo.2007.01.027

Rustioni, G., Audétat, A., & Keppler, H. (2019). Experimental evidence for fluid-induced melting in subduction zones. *Geochemical Perspectives Letters*, *11*, 49–54. https://doi.org/10.7185/geochemlet.1925

Schmidt, C., Rickers, K., Wirth, R., Nasdala, L., & Hanchar, J. M. (2006). Low-temperature Zr mobility: An in situ synchrotron-radiation XRF study of the effect of radiation damage in zircon on the element release in $H_2O + HCl \pm SiO_2$ fluids. *American Mineralogist*, *91*, 1211–1215. https://doi.org/10.2138/am.2006.2244

Schmidt, M. W. (2015). Melting of pelitic sediments at subarc depths: 2. Melt chemistry, viscosities and a parameterization of melt composition. *Chemical Geology*, *404*, 168–182. https://doi.org/10.1016/j.chemgeo.2015.02.013

Schmidt, M. W., & Jagoutz, O. (2017). The global systematics of primitive arc melts. *Geochemistry, Geophysics, Geosystems*. https://doi.org/10.1002/2016GC006699

Schmidt, M. W., & Poli, S. (2014). Devolatilization during subduction. *Treatise on Geochemistry*, *4*, 669–701.

Schmidt, M. W., Vielzeuf, D., & Auzanneau, E. (2004). Melting and dissolution of subducting crust at high pressures: The key role of white mica. *Earth and Planetary Science Letters*, *228*, 65–84. https://doi.org/10.1016/j.epsl.2004.09.020

Shen, A. H., & Keppler, H. (1997). Direct observation of complete miscibility in the albite-H_2O system. *Nature*, *385*, 710. https://doi.org/10.1016/j.epsl.2004.09.020

Shimizu, K., Saal, A. E., Myers, C. E., Nagle, A. N., Hauri, E. H., Forsyth, D. W., et al. (2016). Two-component mantle melting-mixing model for the generation of mid-ocean ridge basalts: Implications for the volatile content of the Pacific upper mantle. *Geochimica et Cosmochimica Acta*, *176*, 44–80. https://doi.org/10.1016/j.gca.2015.10.033

Skora, S., Blundy, J. D., Brooker, R. A., Green, E. C. R., Hoog, J. C. M., & Connolly, J. A. D. (2015). Hydrous phase relations and trace element partitioning behaviour in calcareous sediments at subduction-zone conditions. *Journal of Petrology*, *56*, 953–980. https://doi.org/10.1093/petrology/egv024

Syracuse, E. M., & Abers, G. A. (2006). Global compilation of variations in slab depth beneath arc volcanoes and implications. *Geochemistry, Geophysics, Geosystems*, *7*. https://doi.org/10.1029/2005GC001045

Tropper, P., & Manning, C. E. (2005). Very low solubility of rutile in H_2O at high pressure and temperature, and its implications for Ti mobility in subduction zones. *American Mineralogist*, *90*, 502–505. https://doi.org/10.2138/am.2005.1806

Truckenbrodt, J., & Johannes, W. (1999). *H_2O loss during piston-cylinder experiments* (p. 1333). American Mineralogist. https://doi.org/10.2138/am-1999-0909

Wang, J., Xiong, X., Takahashi, E., Zhang, L., Li, L., & Liu, X. C. (2019). Oxidation state of arc mantle revealed by partitioning of V, Sc, and Ti between mantle minerals and basaltic melts. *Journal of Geophysical Research: Solid Earth*, *124*, e2020JB019452. https://doi.org/10.1029/2018JB016731

Watson, E. B., & Harrison, T. M. (1983). Zircon saturation revisited: Temperature and composition effects in a variety of crustal magma types. *Earth and Planetary Science Letters*, *64*, 295–304. https://doi.org/10.1016/0012-821X(83)90211-X

Wilke, M., Schmidt, C., Dubrail, J., Appel, K., Borchert, M., Kvashnina, K., & Manning, C. E. (2012). Zircon solubility and zirconium complexation in $H_2O + Na_2O + SiO_2 \pm Al_2O_3$ fluids at high pressure. *Earth and Planetary Science Letters*, *349–350*, 15–25. https://doi.org/10.1016/j.epsl.2012.06.054

Workman, R. K., & Hart, S. R. (2005). Major and trace element composition of the depleted MORB mantle (DMM). *Earth and Planetary Science Letters*, *231*, 53–72. https://doi.org/10.1016/j.epsl.2004.12.005

Xiong, X. L., Adam, J., & Green, T. H. (2005). Rutile stability and rutile/melt HFSE partitioning during partial melting of hydrous basalt: Implications for TTG genesis. *Chemical Geology*, *218*, 339–359. https://doi.org/10.1016/j.chemgeo.2005.01.014

Xiong, X. L., Keppler, H., Audétat, A., Gudfinnsson, G., Sun, W., Song, M., et al. (2009). Experimental constraints on rutile saturation during partial melting of metabasalt at the amphibolite to eclogite transition, with applications to TTG genesis. *American Mineralogist*, *94*, 1175–1186. https://doi.org/10.2138/am.2009.3158

Zhang, Z.-M., Shen, K., Sun, W.-D., Liu, Y.-S., Liou, J. G., Shi, C., & Wang, J.-L. (2008). Fluids in deeply subducted continental crust: Petrology, mineral chemistry and fluid inclusion of UHP metamorphic veins from the Sulu orogen, eastern China. *Geochimica et Cosmochimica Acta*, *72*, 3200–3228. https://doi.org/10.1016/j.gca.2008.04.014

Zheng, Y.-F., & Hermann, J. (2014). Geochemistry of continental subduction-zone fluids. *Earth Planets and Space*, *66*, 93. https://doi.org/10.1186/1880-5981-66-93